Advanced Energy Materials

ADVANCED ENERGY MATERIALS
www.advenergymat.de

RESEARCH ARTICLE OPEN ACCESS

Quantifying Evolving Defect Parameters in Metal Halide Perovskites via the Measurement and Modeling of Power-Dependent Transient Photoluminescence

Maxim Simmonds[1] | Yanyan Duan[1] | Manuel F. Vasquez-Montoya[1] | Rowan W. MacQueen[1] | Vincent M. Le Corre[2] | Eva Unger[1] | Thomas Kirchartz[3]

[1]Helmholtz-Zentrum Berlin fur Materialien und Energie GmbH, Berlin, Germany | [2]University of Southern Denmark - Campus Sønderborg, Sønderborg, Denmark | [3]Forschungszentrum Julich GmbH, Jülich, Germany

Correspondence: Maxim Simmonds (maxim.simmonds@helmholtz-berlin.de)

Received: 27 August 2025 | **Revised:** 4 March 2026 | **Accepted:** 5 March 2026

Keywords: carrier dynamics | defect parameters | perovskite defects | time resolved photoluminescence

ABSTRACT

Dynamic photoinduced defect states in metal halide perovskites (MHPs) critically govern the non-equilibrium photophysics, metastability, and long-term performance of optoelectronic devices, such as solar cells. This metastability is evident in steady-state photoluminescence experiments, where the amplitudes increase or decrease depending on the environmental and excitation conditions. Here, we combine excitation-dependent time-resolved photoluminescence (trPL) measurements with parameter estimation via Bayesian optimization coupled with a full Shockley–Read–Hall and diffusion model to quantitatively track defect state formation in $Cs_{0.05}FA_{0.95}PbI_3$ thin films, under continuous 1 sun illumination. This methodology is applied to quantify the evolution of defect distributions in absorbers with two distinct initial optoelectronic qualities, leveraging the sensitivity of trPL decays to defect-assisted non-radiative recombination processes. We show that 21 h of continuous illumination causes the slopes of the differential-lifetime/mean carrier-density plots to converge from initially distinct decay behaviors, which we interpret as a convergence of dominant recombination mechanisms following irradiation. The fitting results further suggest the emergence of trapping species with highly asymmetric capture cross-section ratios. Overall, this study establishes a general diagnostic methodology for tracking carrier-induced degradation pathways in perovskites and other emerging semiconductors.

1 | Introduction

Although metal halide perovskite (MHP)-based photovoltaic devices have reached efficiencies close to their theoretical limit [1, 2], the identification and quantification of their defect parameters and associated chemistry remain limited. For thin-film solar cells, assuming an adequate band-alignment [3], the distribution of defect states ultimately governs the final device performance [4]. With efficiencies approaching the detailed balance limit, attention has increasingly shifted toward device stability [5]. Unlike their inorganic counterparts, MHP absorbers exhibit defect distributions that evolve under continuous stressors such as electrical bias, heat, and illumination, leading to the degradation of external performance parameters [6]. Consequently, a quantitative understanding of how these defect landscapes evolve under stress is crucial for developing devices that satisfy industrial-level reliability standards [7].

Characterizing defect distributions in as-prepared MHP thin films remains a significant challenge [8, 9], as evidenced by the lack of a general consensus on the defect distributions commonly present in perovskite systems. This difficulty arises in

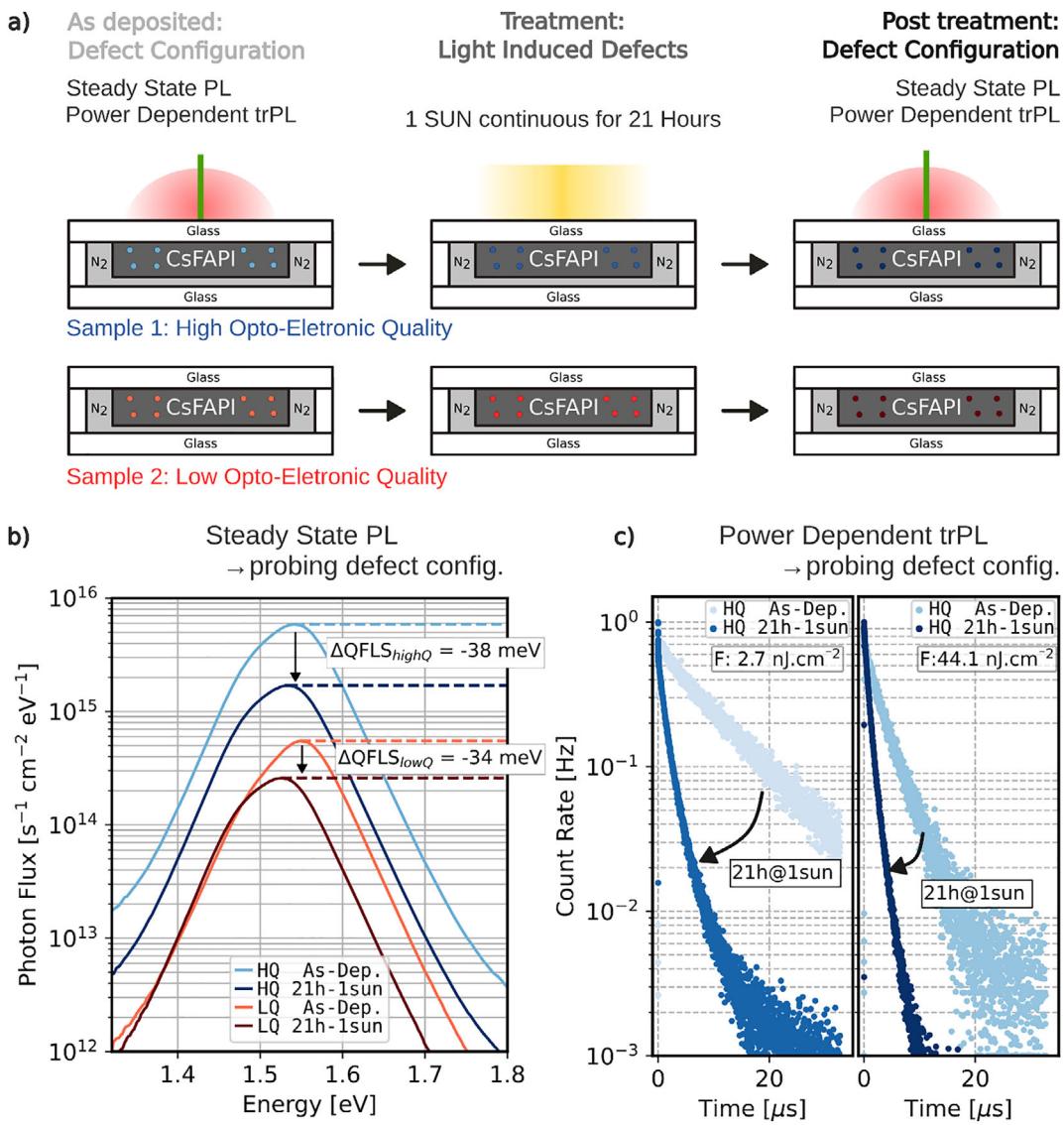

FIGURE 1 | Experimental overview and photoluminescence characterization. (a) Experimental procedure. The arrangement of defects in the high opto-electronic quality (blue) and low opto-electronic quality (red) $Cs_{0.05}FA_{0.95}PbI_3$ thin film samples was measured pre- and post-irradiation using steady-state photoluminescence and power-dependent trPL. As a stressor, we use 21 h of 1 sun (calibrated Xe lamp) irradiation. (b) Steady-state PL of the encapsulated high opto-electronic quality sample (HQ, blue) and low opto-electronic quality (LQ, red). Here, both losses in QFLS are comparable. (c) Example of power-dependent trPL measurements (HQ). 21 h of irradiation leads to much faster decays, pointing to higher non-radiative recombination rates.

part from the strong sensitivity of MHPs to synthesis conditions and procedures [10, 11], leading to a broad range of emergent as-prepared optoelectronic properties. Furthermore, under continuous external stressors such as heat, moisture, bias, and light, MHP materials undergo various (ir)reversible chemical reactions [12]. These processes further modify the defect distributions, complicating efforts to reliably characterize recombination-active defects and their evolution over time.

Despite these challenges, recent modeling efforts applied to optical measurements of MHP thin films, such as frequency-dependent photoluminescence quantum yield (PLQY) [13], long-decaying time-resolved photoluminescence (trPL) [14], and power-dependent trPL [15], consistently highlight that a complex arrangement of trap states is necessary to correctly describe transient (or steady-state) power-dependent photoluminescence behavior. These models generally agree on the presence of shallow traps, leading to so-called photodoping effects upon carrier injection [16]. However, significant disagreement remains regarding the energy positions of the traps, whether they are acceptor or donor traps, or the specific defect structures that correspond to the defect parameters extracted from optical measurements.

Evidence for time-dependent defect distribution in perovskite thin-film absorbers has also been observed predominantly through variations in steady-state photoluminescence (PL) intensity. Depending on experimental conditions, PL intensity can increase or decrease depending on the conditions of continuous illumination [17–19] or quasi-continuous illumination [20]. These studies further highlight the crucial role of the sample environ-

ment in the PL evolution under continuous illumination [21]. The prevailing interpretation is that the free carriers introduce or annihilate trapping sites, causing a drop or increase in PL intensity during irradiation [17–21]. While correlations to kinetic models and DFT calculations have been shown previously [20], the quantitative parameters of these photoinduced trapping sites and their direct impact on recombination dynamics remain insufficiently resolved.

In this study, to probe systems with different initial defect distributions, we investigate two twin batches of nominally identical cesium(5%)-formamidinium(95%)-lead iodide ($Cs_{0.05}FA_{0.95}PbI_3$, CsFAPI) thin films deposited on quartz substrates. The samples differ in their initial optoelectronic quality, as assessed by steady-state photoluminescence, and are subsequently subjected to 21 h of continuous 1 sun illumination. In the following, we focus on the formation and evolution of trap states induced by continuous irradiation.

Because power-dependent trPL measurements are particularly sensitive to defect-mediated recombination, we advance prior steady-state PL investigations by combining power-dependent trPL measurements with modeling that includes Shockley–Read–Hall (SRH) trapping–detrapping statistics and carrier diffusion. By fitting the experimental data using Bayesian optimization, we attempt to quantitatively track the evolution of defect populations in MHP absorbers under irradiation. These results establish a quantitative framework for studying the evolution of defect landscapes in 3D semiconductors.

2 | Results and Discussion

2.1 | Visualizing the Evolution of the Defect Landscape via Steady-State PL and Power-Dependent trPL

Figure 1a illustrates the experimental procedure followed by two nominally identical $Cs_{0.05}FA_{0.95}PbI_3$ thin films on quartz glass and encapsulated with UV curable glue and cavity glass. From the absolute steady-state PL spectrum in Figure 1b, we extract a quasi-fermi level splitting (QFLS) of 1.166 eV (as deposited, blue) and 1.110 eV (as deposited, red) using the high-energy fit method [22]. As the blue and red samples exhibit a higher and lower initial QFLS, we refer to them as high- and low-opto-electronic quality samples, abbreviated as HQ or LQ, respectively. Figure S2 shows the XRD spectra for the HQ and LQ samples. For the HQ sample, a higher amount of crystalline PbI_2 is incorporated within the material, in line with empirical observations that a small excess of lead-iodide enhances opto-electronic quality [23, 24].

For both samples, a low-energy shoulder is observed in the PL spectrum. Such features have recently been discussed in detail and attributed to photon reabsorption effects, which can give rise to pronounced low-energy shoulders in measured PL spectra [25]. In the as-deposited state, the LQ sample exhibits a less pronounced low-energy shoulder, which we attribute to reduced photon reabsorption due to increased surface roughness. This interpretation is corroborated by the cross-sectional SEM images shown in Figure S3, where a rougher surface morphology is observed for the LQ sample. Following irradiation, both samples exhibit a reduction in QFLS of 38 meV (HQ) and 34 meV (LQ), respectively. Additionally, an enhanced low-energy shoulder is observed for both samples (Figure S4, left panel), suggesting changes in the optical geometry and/or the contribution of additional sub-bandgap, defect-related emission.

Taken together, these observations point to an increase in non-radiative recombination pathways in both samples due to continuous irradiation with 1 sun.

2.2 | Power Dependent trPL: Before and After 1 Sun Continuous Irradiation

To probe the evolution of the defect landscape, we measure power-dependent trPL before and after exposure, as it is particularly sensitive to defect-mediated recombination pathways. Varying the excitation fluence allows access to a broad range of carrier densities during the decay, thereby enhancing sensitivity to distinct recombination regimes. Indeed, since the rates of radiative and SRH recombination depend solely on the electron and hole densities (see Equations S2.1–S2.4), probing a material over a broad range of carrier densities allows distinct recombination regimes to emerge. Each regime is associated with different recombination processes, such as non-radiative recombination dominated by a certain type of trap [26], or direct band-to-band radiative recombination. By fitting the resulting decay dynamics with compatible kinetic models, we attempt to extract quantitative information about the trap distribution [14, 15] and assess changes in optoelectronic quality. An example is depicted in Figure 1c), for the HQ sample. Pre-irradiation is shown in light blue and post-irradiation in dark blue. There, the post-irradiation traces decay much faster than the pre-irradiation traces, showing the emergence of non-radiative pathways in the treated sample owing to continuous irradiation.

We first focus on the early-time PL decay ($t < 20$ ns). As shown in Figure S5, the fluence dependence of the initial PL peak (at $t = 0$) follows an $PL(0) \propto n^2$ slope, indicating that for all conditions, the samples are intrinsic and display very low doping. After the initial PL peak, a fast initial decay is observed. This initial decay is governed by two main processes that result in a fast initial drop in PL intensity: (a) carrier diffusion from an initial Beer-Lambert carrier density profile toward a homogeneous profile, and (b) fast trap-filling events, where photogenerated charge carriers are captured by pre-existing shallow trap states, rendering them unavailable for radiative recombination. From the measured absorption coefficients of our samples (Figure S1), we estimate that diffusion alone accounts for approximately 40% of the measured initial drop (see horizontal line of Figure S6). There, we observe larger drops at lower fluences, both processes (a) and (b) are likely to contribute to the initial PL drop.

Figure S6 presents the early-time trPL decays for the four experimental conditions. For the as-deposited HQ sample (Figure S6a), the magnitude of the initial PL drop shows only a weak dependence on excitation fluence. After 21 h of continuous irradiation (top-right panel, Figure S6a), a substantially faster early-time decay is observed at low fluence, consistent with the

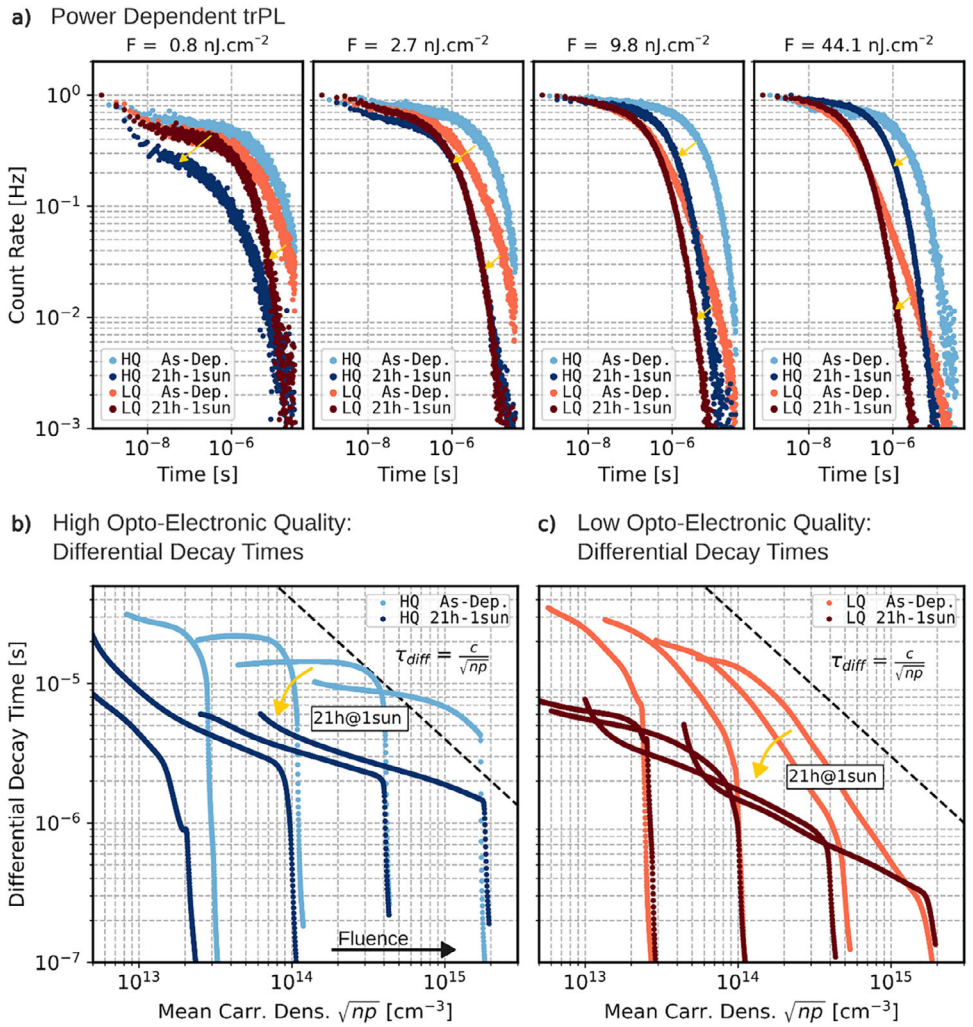

FIGURE 2 | Power-dependent trPL decays for the HQ and LQ samples in (a). We observe systematically faster decays after irradiation (dark blue and dark red). Differential decay time plots as a function of the estimated mean carrier density for (b) HQ and (c) LQ. These plots are derived from the trPL data of (a), where τ_{diff} corresponds to an instantaneous exponential slope. The slope $\tau_{\text{diff}}(n) \propto \sqrt{np}^{-1}$ was previously described analytically for a sufficiently shallow single trap level [14]. Following irradiation, both samples exhibit similar slopes at low carrier densities, indicating comparable dominant recombination regimes.

formation of fast-filling shallow trapping sites. At higher excitation fluences (darker traces), the fraction of carriers captured by shallow traps becomes small relative to the total photogenerated carrier population, resulting in a reduced initial PL drop (Figure S6b). In contrast, the LQ sample exhibits a pronounced early-time PL drop both before and after irradiation.

These observations indicate that continuous irradiation induces an additional fast-filling trapping species in the HQ sample, whereas these fast-filling traps are already present in the as-deposited LQ sample and persist following irradiation.

To better observe changes in dominant recombination regimes before and after irradiation, we plot the differential decay times as a function of carrier density, extracted from the power-dependent trPL measurements shown in Figure 2a. The differential decay time is the corresponding exponential slope at each point in time of a PL decay. Plotting it against the carrier density highlights the dominant recombination mechanisms involved, as the recombination rates solely depend on the carrier density and recombination coefficients. This method is gaining recognition as a valuable tool for identifying recombination mechanisms in perovskite thin films as they display complex, non-single-, non-bi-, or non-tri-exponential trPL decays. The differential decay time is defined as [14]:

$$\tau_{\text{diff}} = -2\left(\frac{d\ln(\phi_{\text{PL}})}{dt}\right)^{-1}$$

where ϕ_{PL} is the PL intensity. Such differentiation often needs an initial smoothing step to avoid large deviations of τ_{diff}. In our case, an arbitrary number of eight exponentials was fitted to the experimental data before differentiation. The geometric mean of the carrier density:

$$\sqrt{n(t)\,p(t)} = n_{0,est}\sqrt{\phi_{\text{PL,norm}}(t)}$$

is then obtained from the normalized PL. Here, $n_{0,est}$ is the estimated initial carrier density (see Supporting Information p.2).

For an intrinsic semiconductor without photodoping ($n = p$), the geometric mean simplifies to $\sqrt{n(t)p(t)} = n(t)$. In Figure 2, we also include a guide for the eye, defined by $\tau_{\mathrm{diff}} \propto \sqrt{np}^{-1}$, the only slope predicted analytically for a sufficiently shallow single trap level [14].

The differential decay times are shown in Figures 2b,c. Each trPL decay progresses from right to left, starting at high carrier densities on the lower right (corresponding to a PL maximum) and moving toward the upper left as the carriers recombine.

In Figure 2b, the HQ sample exhibits two regimes for all decay curves: (i) a rapid initial increase at high densities, corresponding to the steep decrease in the PL shown in Figure S6, reflecting diffusion and shallow trapping of photogenerated carriers, which is followed by (ii) a weaker slope distinct from the analytical n^{-1} slope. After irradiation, in darker blue, we observe a change in the slopes for the second regime, with all decays converging to that one. Here, we observe a change in the dominating recombination regime due to irradiation. Lower average decay times also point to an increase in recombination rates.

For the LQ sample, as shown in Figure 2c, three regimes occur before irradiation: (i) a rapid initial, diffusion/shallow-trapping-related increase at high densities, (ii) an intermediate, stronger slope, and (iii) a weaker slope at the lowest densities. After irradiation, in darker red, the second stronger slope disappears, with only the weaker slope (iii) remaining. Again, we see that the dominating recombination pathways have changed due to irradiation. That said, as the weaker slope was already present at lower densities before irradiation, we can conclude that the trapping species dominating recombination after irradiation were already present before.

We observe that both samples evolve toward similar recombination regimes after irradiation, as evidenced by the overlap of the low–carrier-density slopes in the differential decay-time plots following irradiation (Figure S7b compared to Figure S7a). This convergence indicates that initially distinct samples develop comparable dominant recombination pathways under prolonged 1 sun illumination. Notably, the LQ sample exhibits consistently shorter average differential decay times after irradiation. Under the assumption that recombination is dominated by a single trapping species, this behavior suggests a higher density of the corresponding recombination-active defects in the LQ sample at the end of the irradiation treatment.

Additionally, these changes appear to be long-lived: As shown in Figure S8, the reduced differential lifetime slope observed after irradiation for the HQ sample persists even after 100 h of storage in a nitrogen environment, with a slight recovery of overall lifetime values.

Finally, the above analysis is shown (see Figure S9) to be a powerful methodology for discriminating qualitatively different dominant recombination mechanisms across samples that are nominally identical but subject to external batch-to-batch variations. This approach makes characteristic sample-specific signatures more accessible, enabling deeper rationalization of differences in pre-existing defect parameters and their evolution under external stress.

2.3 | Evolving Defect Landscape Due to Continuous Irradiation: Modeling and Discussion

Since the differences in photoluminescence (PL) decay dynamics arise from changes in defect populations, we model them with a set of coupled rate equations. The model includes a radiative recombination term as well as the full Shockley–Read–Hall (SRH) formalism [28]. Owing to the relatively low excitation fluences used in our experiments ($F < 45$ nJ cm^{-2}), the Auger recombination term is neglected (see Note S2). To capture all processes during the early PL drop (as explained above), we add a diffusion term allowing for the diffusion of carriers through the film thickness in the out-of-plane direction (see Supporting Information: Theory for a detailed description of the model and fitting procedures).

Related rate-equation approaches have previously been applied to metal halide perovskite thin films, although typically using simplified SRH formulations [15]. Recent first-principles studies have demonstrated that strong lattice anharmonicity in lead-halide perovskites leads to a breakdown of the conventional correlation (as seen in inorganic semiconductors) between trap energy levels and capture cross-sections [29]. Consequently, a much broader range of physically plausible combinations of trap energies and carrier capture coefficients can occur, rendering common SRH simplifications effectively arbitrary in these materials. For instance, assumptions commonly associated with shallow traps—where one carrier capture cross-section is expected to be dominant while the opposite carrier capture is negligibly small—are not generally valid in metal halide perovskite semiconductors [29]. Therefore, we employ the full SRH formalism to describe trPL decays and explicitly allow for unconventional combinations of trap energies and capture coefficients. Finally, we ensure that the model reproduces the experimentally observed power dependence of the PL response (see Figure S5). Such an approach has recently been used to describe the power-law nature of perovskite thin films, albeit without the need for diffusion terms [14].

The use of the full SRH formalism significantly increases the dimensionality of the parameter space compared to simplified models. For each trapping species, four independent parameters are required: the trap density N_t [cm^{-3}], the electron and hole capture coefficients β_n [cm^3 s^{-1}] and β_p [cm^3 s^{-1}] respectively, and the trap depth E_t [eV] defined relative to the valence band. For the rest of the analysis, we assume the traps to be acceptor-like traps closer to the conduction band, which leads to the correct fluence-dependent slope of 2 of Figure S5, corresponding to high injection conditions and interpreted as low doping densities. This choice is arbitrary, and a symmetric case with donor traps equidistant from the valence band would yield identical dynamics.

To efficiently explore the expanded parameter space, we employ Bayesian optimization using the code provided by the optimPV library [30]. For each sample, four trPL decays acquired at different excitation fluences—spanning approximately two orders of magnitude—are fitted simultaneously using a global optimization procedure. As shown in Figure S10, increasing the number of trapping species beyond two does not lead to a significant improvement in the fit quality, as seen by the normalized root

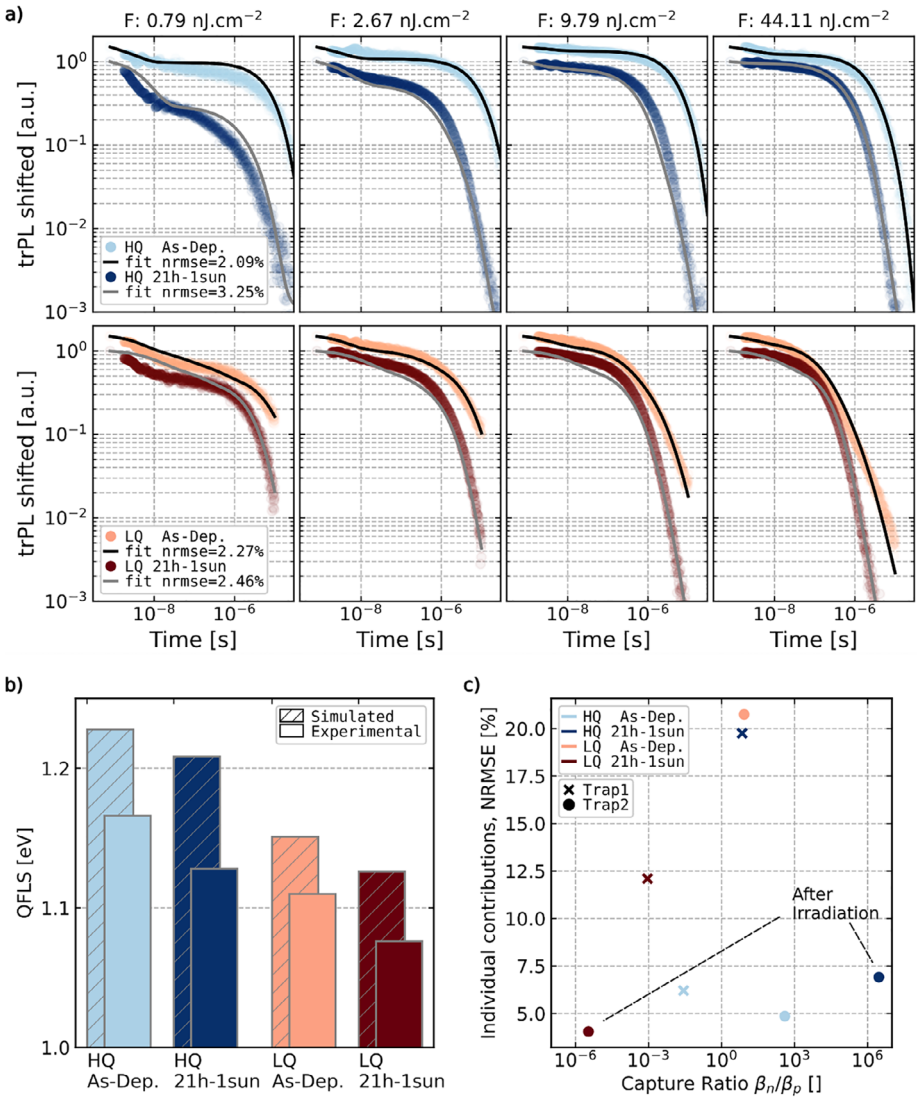

FIGURE 3 | Fitting results and parameter analysis for all sample conditions. (a) Global fits for the HQ (top, blue) and LQ (bottom, red) samples. The black curves correspond to the fits for the as-deposited conditions, while the grey curves show the after-irradiation conditions. In each case, a single set of fit parameters is used to model the four excitation fluences simultaneously. (b) Simulated quasi-Fermi level splitting (QFLS) under 1 sun illumination using the fitted parameters from panel (a). The experimentally measured QFLS values are shown as solid boxes. (c) Normalized root mean square error (NRMSE) obtained when retaining only a single trapping species from the fits in panel (a). The capture cross-section ratio β_n/β_p, previously proposed as an indicator of trap type [27], is shown on the horizontal axis. After irradiation, the trapping species associated with the lowest NRMSE values exhibit highly asymmetric capture cross-section ratios (on the order of 10^6 or 10^{-6}).

mean square error (NRMSE). Therefore, we restrict the fitting to two trap species per condition.

The best results are presented in Figure 3a, where the as-deposited fits are plotted in black, and the irradiated fits in grey. With NRMSE around 0.2 to 0.3, we judge the fits to be satisfactory, with discrepancies still visible for certain conditions at early times (e.g., the early times of the LQ after-irradiation condition, dark red data—grey fit couple).

To identify the trapping species introduced upon irradiation, we analyze the individual contributions of each trap to the overall fit by plotting, in Figure 3c, the normalized root mean square error (NRMSE) obtained when only a single trapping species is included in the model. In this representation, lower NRMSE values correspond to trapping species that contribute more strongly to the reproduction of experimental trPL decays. The horizontal axis shows the ratio β_n/β_p (or equivalently, β_p/β_n), a quantity previously proposed as an indicator of trap type [27]. Therefore, this analysis discriminates between trap types that significantly contribute to the observed trPL dynamics.

As shown, after irradiation, both the HQ and LQ samples exhibit trapping species with a β_n/β_p ratio of 10^6 and $10^{-6,}$ respectively, that yield low NRMSE values and thus provide better agreement with the experimental data.

The corresponding simulated differential decay curves associated with the single-trap NRMSE contributions shown in Figure 3c

are presented in Figure S11. In this figure, the grey solid lines represent simulations including both trapping species, while the dashed pink and green lines show the contributions arising from trap 1 and trap 2 individually, respectively.

For the HQ sample measured after irradiation (Figure S11a), the single-trap contributions reproduce the experimental data only over a limited time window at intermediate times for the high fluence, indicating that the overall decay dynamics cannot be described by one of the fitted trapping species alone but instead require the combined contribution of both traps. For the LQ sample after irradiation (Figure S11b), a more pronounced overlap is observed between the experimental data and the contribution from trap 2 alone, with discrepancies emerging primarily at lower carrier densities, similar to the behavior observed for the HQ sample. As discussed previously (Figure 3c), trap 2 is characterized by a capture cross-section ratio β_n/β_p of approximately 10^6 for HQ and 10^{-6} for the LQ sample. We conclude here that continuous irradiation leads to the emergence of a high density of trapping states with asymmetric capture cross sections.

Figure 3b displays the simulated steady-state quasi-Fermi level splitting (QFLS) under 1 sun illumination (see Section S4 for details), along with the corresponding experimental values. The simulations systematically overestimate the absolute QFLS by approximately 50–80 meV. An examination of the associated steady-state recombination rates to each trap (Figure S12) reveals that the traps dominating recombination are not characterized by more symmetric capture cross-section ratios ($\beta_p/\beta_n \approx 1$), as would be expected within the SRH framework. Instead, as discussed above, the trapping species that predominantly describe the trPL decays at intermediate times are characterized by highly asymmetric capture cross-section ratios ($\beta_p/\beta_n \approx 10^6$ or 10^{-6}). We therefore suggest that more accurate fits at early and long-times would play an important role in accurately linking transient recombination processes to steady-state defect-mediated recombination within the films.

At present, it remains unclear whether the observed variations in the trap type reflect long-term modifications of recombination-active defects within the material or arise, at least in part, from artifacts associated with the generalized fitting procedure. Moreover, the classical SRH formalism employed here does not explicitly account for changes in trapping properties due to defect filling. This limitation can be addressed by adopting the Sah–Shockley [31] approach, which extends SRH theory to defects with multiple charge states and is consistent with theoretical predictions of defect states with multiple charged states in metal halide perovskites [32].

Overall, these findings highlight the sensitivity of power-dependent trPL measurements to changes in the defect parameters for MHP thin films. We also demonstrate the capability of modeling procedures for analyzing and fitting experimental curves. Beyond quantifying trap dynamics, the results point toward the need for further understanding of defect chemistry as a key factor affecting transient PL responses in relation to defect stability in perovskite thin films. More broadly, owing to its generality, such methodology and modeling are also applicable to the determination of the complex arrangement of defects in a wide range of 3D semiconductors.

3 | Conclusions

In this study, we present a quantitative investigation of the long-term evolution of defect landscapes in thin films under quasi-continuous near-band-edge illumination. Power-dependent time-resolved photoluminescence (trPL) measurements show that continuous light exposure increases non-radiative recombination, with these changes persisting for over 100 h with slight recovery.

Differential decay-time analysis reveals similar responses to illumination stress depending on the starting optoelectronic quality of the material. Both samples see their dominating recombination mechanisms converge, as evidenced by their comparable differential decay time slopes.

Using an extended Shockley–Read–Hall (SRH) + diffusion model with Bayesian optimization as the fitting algorithm, we attempt to identify the nature of these newly introduced traps and quantify their parameters. By isolating the trapping species that contribute most strongly to reproducing the experimental TRPL decays, we assign the light-induced defects to traps characterized by a highly asymmetric capture cross-section ratio, previously proposed as an indicator of trap type.

Further simulations of the steady-state response using the fitted parameters highlight the importance of accurately capturing both the low-fluence regime and the early-time dynamics of the TRPL decays. These results raise the question of which excitation fluences and temporal regions of perovskite TRPL decays are most critical for reliably extracting defect parameters relevant to steady-state operation.

The modeling framework successfully captures the evolution of trap-mediated recombination pathways with a set of physically interpretable traps, reproducing complex PL transients over two orders of magnitude in fluence. The emergence of additional traps highlights the sensitivity of the PL decay profiles to changes in the defect distribution. These findings demonstrate the predictive capability of the SRH + diffusion models for interpreting complex trPL data. Further insights into the varied defect landscapes of metal halide perovskites are needed to establish the use of trPL as a diagnostic tool for the evaluation of perovskite stability.

In a broader context, we highlight the importance of *charge carrier chemistry*, specifically how photogenerated carriers mediate the formation, transformation, and occupation of defect states. Understanding carrier-defect interactions is essential for developing accurate kinetic models of perovskite thin films, which can ultimately guide the design of resilient materials and interfaces for stable perovskite-based devices.

Acknowledgements

M.S. is grateful for the support by the German–Israeli Helmholtz International Research School HI-SCORE (HIRS-0008). M.S. thanks Shengnan Zuo for her support during sample preparation. M.S., Y.D. and M.V. thank J. Beckedahl, M. Choyne., C. Ferber, M. Wittig, T. Lußky, and H. Heinz for the technical support in HySPRINT Photovoltaic Lab. A part of this

work has been supported by the Helmholtz Association in the framework of the Solar Technology Acceleration Platform (Solar TAP), Grant No. 714-62150-3. V.M.L.C. acknowledges support from the Villum Foundation, Grant No. 50440. T.K. acknowledges funding by the Helmholtz Association via the POF IV funding, via the project "Beschleunigter Transfer der nächsten Generation von Solarzellen in die Massenfertigung—Zukunftstechnologie Tandem-Solarzellen", via the Helmholtz.AI project AISPA—AI-driven instantaneous solar cell property analysis as well as by the Deutsche Forschungsgemeinschaft (German Research Foundation) via the project "Correlating Defect Densities with Recombination Losses in Halide-Perovskite Solar Cells."

Open access funding enabled and organized by Projekt DEAL.

Conflicts of Interest

The authors declare no conflicts of interest.

Data Availability Statement

All the experimental data and codes linked to the data analysis is openly available in this repository: https://github.com/MimaxSimm/trPL-Fitting.

References

1. O. Almora, G. C. Bazan, C. I. Cabrera, et al., "Device Performance of Emerging Photovoltaic Materials (Version 5)," *Advanced Energy Materials* 15 (2025): 2404386, https://doi.org/10.1002/aenm.202404386.

2. T. Kirchartz, G. Yan, Y. Yuan, B. K. Patel, D. Cahen, and P. K. Nayak, "The state of the Art in Photovoltaic Materials and Device Research," *Nature Reviews Materials* 10 (2025): 335–354, https://doi.org/10.1038/s41578-025-00784-4.

3. M. Stolterfoht, P. Caprioglio, C. M. Wolff, et al., "The Impact of Energy Alignment and Interfacial Recombination on the Internal and External Open-Circuit Voltage of Perovskite Solar Cells," *Energy & Environmental Science* 12 (2019): 2778–2788, https://doi.org/10.1039/C9EE02020A.

4. O. Breitenstein, J. Bauer, P. P. Altermatt, and K. Ramspeck, "Influence of Defects on Solar Cell Characteristics," *Solid State Phenomena* 156–158 (2009): 1–10.

5. H. Zhu, S. Teale, M. N. Lintangpradipto, et al., "Long-Term Operating Stability in Perovskite Photovoltaics," *Nature Reviews Materials* 8 (2023): 569–586, https://doi.org/10.1038/s41578-023-00582-w.

6. A. Levtchenko, A. Julien, D. McDermott, et al., "Coupled In Situ Electrical and Optical Characterization to Assess the Accelerated Aging of Perovskite Solar Cells," *Solar RRL* 8 (2024): 2400511.

7. P. Holzhey, M. Prettl, S. Collavini, N. L. Chang, and M. Saliba, "Toward Commercialization with Lightweight, Flexible Perovskite Solar Cells for Residential Photovoltaics," *Joule* 7 (2023): 257–271, https://doi.org/10.1016/j.joule.2022.12.012.

8. T. Kirchartz, "Challenges and Opportunities for the Characterization of Electronic Properties in Halide Perovskite Solar Cells," *Chemical Science* 16 (2025): 8153–8195, https://doi.org/10.1039/D5SC00504C.

9. M. C. Schmidt and B. Ehrler, "How Many Mobile Ions Can Electrical Measurements Detect in Perovskite Solar Cells?" *ACS Energy Letters* 10 (2025): 2457–2460, https://doi.org/10.1021/acsenergylett.5c00887.

10. L. Zimmermann, D. Menzel, R. Gundermann, et al., "Unveiling the Impact of C_{60}–O_2 Interaction on the Performance and Characterization of Perovskite Solar Cells," *Advanced Energy Materials* 15 (2025): 2501225, https://doi.org/10.1002/aenm.202501225.

11. E. R. Nandayapa, K. Hirselandt, C. Boeffel, E. L. Unger, and E. J. W. List-Kratochvil, "Unraveling Reversible Quenching Processes of O_2, N_2, Ar, and H_2O in Metal Halide Perovskites at Moderate Photon Flux Densities," *Advanced Optical Materials* 9 (2021): 2001317, https://doi.org/10.1002/adom.202001317.

12. J. Zhuang, J. Wang, and F. Yan, "Review on Chemical Stability of Lead Halide Perovskite Solar Cells," *Nano-Micro Letters* 15 (2023): 84, https://doi.org/10.1007/s40820-023-01046-0.

13. A. Kiligaridis, P. A. Frantsuzov, A. Yangui, et al., "Are Shockley-Read-Hall and ABC Models Valid for Lead Halide Perovskites?," *Nature Communications* 12 (2021): 3329, https://doi.org/10.1038/s41467-021-23275-w.

14. Y. Yuan, G. Yan, C. Dreessen, et al., "Shallow Defects and Variable Photoluminescence Decay Times up to 280 µs in Triple-cation Perovskites," *Nature Materials* 23 (2024): 391–397, https://doi.org/10.1038/s41563-023-01771-2.

15. M. Kober-Czerny, A. Dasgupta, S. Seo, et al., "Determining Parameters of Metal-Halide Perovskites Using Photoluminescence with Bayesian Inference," *PRX Energy* 4 (2025): 013001, https://doi.org/10.1103/PRXEnergy.4.013001.

16. A. Marunchenko, J. Kumar, A. Kiligaridis, et al., "Charge Trapping and Defect Dynamics as Origin of Memory Effects in Metal Halide Perovskite Memlumors," *The Journal of Physical Chemistry Letters* 15 (2024): 6256–6265, https://doi.org/10.1021/acs.jpclett.4c00985.

17. Y. Chen, T. Wang, Z. Li, et al., "Communicating Two States in Perovskite Revealed by Time-Resolved Photoluminescence Spectroscopy," *Scientific Reports* 8 (2018): 16482, https://doi.org/10.1038/s41598-018-34645-8.

18. S. Chen, X. Wen, S. Huang, et al., "Light Illumination Induced Photoluminescence Enhancement and Quenching in Lead Halide Perovskite," *Solar RRL* 1 (2017): 1600001, https://doi.org/10.1002/solr.201600001.

19. Z. Andaji-Garmaroudi, M. Anaya, A. J. Pearson, and S. D. Stranks, "Photobrightening in Lead Halide Perovskites: Observations, Mechanisms, and Future Potential," *Advanced Energy Materials* 10 (2020): 1903109, https://doi.org/10.1002/aenm.201903109.

20. S. G. Motti, D. Meggiolaro, A. J. Barker, et al., "Controlling Competing Photochemical Reactions Stabilizes Perovskite Solar Cells," *Nature Photonics* 13 (2019): 532–539, https://doi.org/10.1038/s41566-019-0435-1.

21. J. F. Galisteo-López, M. E. Calvo, and H. Míguez, "The Complex Interplay of Lead Halide Perovskites with Their Surroundings," *Advanced Optical Materials* 9 (2021): 2100133, https://doi.org/10.1002/adom.202100133.

22. T. Kirchartz, J. A. Márquez, M. Stolterfoht, and T. Unold, "Photoluminescence-Based Characterization of Halide Perovskites for Photovoltaics," *Advanced Energy Materials* 10 (2020): 1904134, https://doi.org/10.1002/aenm.201904134.

23. X. Wang, J. Li, R. Guo, et al., "Regulating Phase Homogeneity by Self-Assembled Molecules for Enhanced Efficiency and Stability of Inverted Perovskite Solar Cells," *Nature Photonics* 18 (2024): 1269–1275, https://doi.org/10.1038/s41566-024-01531-x.

24. Z. Li, X. Sun, X. Zheng, et al., "Stabilized Hole-Selective Layer for High-Performance Inverted p-i-n Perovskite Solar Cells," *Science* 382 (2023): 284–289, https://doi.org/10.1126/science.ade9637.

25. P. Fassl, V. Lami, F. J. Berger, et al., "Revealing the Internal Luminescence Quantum Efficiency of Perovskite Films via Accurate Quantification of Photon Recycling," *Matter* 4 (2021): 1391–1412.

26. J. Hüpkes, U. Rau, and T. Kirchartz, "Impact of Trap Depth on the Steady-State and Transient Photoluminescence in Halide Perovskite Films," *Advanced Energy Materials* 15 (2025): 03157.

27. J. G. Simmons and G. W. Taylor, "Nonequilibrium Steady-State Statistics and Associated Effects for Insulators and Semiconductors Containing an Arbitrary Distribution of Traps," *Physical Review B* 4 (1971): 502–511, https://doi.org/10.1103/PhysRevB.4.502.

28. W. Shockley and W. T. Read Jr., "Statistics of the Recombination of Holes and Electrons," *Physical Review* 87 (1952): 835.

29. X. Zhang, M. E. Turiansky, J.-X. Shen, and C. G. Van De Walle, "Defect Tolerance in Halide Perovskites: A First-Principles Perspective," *Journal of Applied Physics* 131 (2022): 090901, https://doi.org/10.1063/5.0083686.

30. V. M. Le Corre and L. Lüer, "optimPV: Optimization and Modeling Tools for Photovoltaics Research," GitHub repository, 2026, https://github.com/openPV-lab/optimPV, (accessed on 23/01/2026).

31. C.-T. Sah and W. Shockley, "Electron-Hole Recombination Statistics in Semiconductors Through Flaws with Many Charge Conditions," *Physical Review* 109 (1958): 1103–1115, https://doi.org/10.1103/PhysRev.109.1103.

32. D. Meggiolaro, S. G. Motti, E. Mosconi, et al., "Iodine Chemistry Determines the Defect Tolerance of Lead-Halide Perovskites," *Energy & Environmental Science* 11 (2018): 702–713, https://doi.org/10.1039/C8EE00124C.

Supporting Information

Additional supporting information can be found online in the Supporting Information section.

Supporting File: aenm70830-sup-0001-SuppMat.pdf.